Published in final edited form as:
Opt Lett. 2010 July 1; 35(13): 2121–2123.

Time-resolved diffuse optical tomography with patterned-light illumination and detection

Jin Chen[1], **Vivek Venugopal**[1], **Frederic Lesage**[2], and **Xavier Intes**[1,*]

[1]Department of Biomedical Engineering, Rensselaer Polytechnic Institute, Troy, New York 12180, USA

[2]Département de Génie Électrique et Institut de Génie Biomédical, École Polytechnique de Montréal, Québec H3C 3A7, Canada

Abstract

This investigation explores the feasibility of performing diffuse optical tomography based on time-domain wide-field illumination and detection strategies. Wide-field patterned excitation and detection schemes are investigated in transmittance geometry with time-gated detection channels. A Monte Carlo forward model is employed to compute the time-resolved Jacobians for rigorous light propagation modeling. We demonstrate both *in silico* and experimentally that reconstructions of absorption structures based on wide-field patterned-light strategies are feasible and outperform classical point excitation schemes for similar data set sizes. Moreover, we demonstrate that time-domain information is retained even though large spatial areas are illuminated. The enhanced time-domain data set allows for quantitative three-dimensional imaging in thick tissue based on relatively small data sets associated with much shorter acquisition times.

Diffuse optical tomography (DOT) has been extensively explored for clinical functional imaging applications, such as optical mammography [1,2], neuroimaging [3], and muscle imaging [4]. Recently, a new approach to perform 3D volumetric imaging of thick tissue based on structured illumination has been proposed by Cuccia *et al.* [5]. By analyzing the frequency-dependent optical intensities, the optical properties of the medium can be quantitatively estimated and the depth sensitivity of detection inside the turbid medium can be controlled by varying the spatial frequency of the illumination pattern. The method was extended to DOT using Fourier analysis either with simulations in continuous mode [6] or experimentally in the frequency domain [7]. Furthermore, Belanger *et al.* [8] demonstrated that the wide-field structured illumination strategy could be applied to the detection channel for real-time DOT using only a single detector.

In this Letter, we investigate the application of patterned-light illumination and detection strategies to the time domain. In particular, we investigate for the first time the performance of DOT based on time-domain data sets acquired with simple wide-field patterns. The rationale for this work is that the benefits of time-domain tomography observed in point

---

[*] Corresponding author: intesx@rpi.edu.
J. Chen and V. Venugopal contributed equally to the work.

OCIS codes: 170.3010, 170.6920, 170.6960, 170.3880.

illumination/detection schemes may not readily translate to patterned configurations as the temporal information may be reduced due to the spatial extent of the excitation and detection. Moreover, the application of pattern detection strategies to the time domain has not been investigated yet. First, we establish the merit of the approach *in silico* and compare the performances of point and patterned-light strategies quantitatively. Second, we demonstrate experimentally the potential of a wide-field structured light illumination and detection scheme for quantitative three-dimensional (3D) imaging of absorptive heterogeneities in a murine like geometry.

The investigations discussed in this Letter employ a basic pattern scheme based on a previous study [8]. The patterns represent a large vertical or horizontal bar sliding over the volume of the imaged area (1/2 of the surface is illuminated at any pattern). It may be noted that these patterns do not replicate Fourier modes that are generally sinusoidal in nature. Such simple patterns are easier to implement experimentally, owing to faster switching time due to the absence of gray levels and, moreover, can easily be applied to complex geometries.

For the *in silico* studies, a complex absorptive inclusion was simulated within a homogenous medium of size 32 × 32 mm and thickness 20 mm [c.f. Fig. 1(a)]. The background optical properties were set to replicate the optical properties of the experimental settings described in the next paragraph. The absorption heterogeneity had a contrast of 2. The complex absorption structure was positioned in the center of the volume with a thickness of 4 mm. A newly developed Monte Carlo code was employed to accurately compute the forward model and associated Jacobians in the case of complex illumination and detection schemes [9]. Three experimental strategies were simulated: point source–point detector (• + •), pattern illumination–point detector (□ + •), and pattern illumination–pattern detection (□ + ⊡). A 2 × 2 cm area (relevant to small animal imaging) was considered for excitation and detection with evenly spanning point sources–detectors pairs. In all *in silico* cases herein, the total number of excitation sources/illumination patterns and point detectors/detection patterns was set to 36 leading to 1296 combinations (• + •:36 point source × 36 point detectors, □ + •:36 excitation patterns × 36 point detectors, and □ + ⊡:36 excitation × 36 detection patterns).

For *in vitro* studies, a polycarbonate tank of dimensions 80 mm × 50 mm × 20 mm was filled with a mixture of Intralipid-20% (Sigma-Aldrich, USA) diluted in water and India Ink to simulate bulk murine tissue optical parameters ($\mu_a = 0.005$ mm^{-1} and $\mu_s' = 1.16$ mm^{-1}). The phantom holds three cylindrical glass inclusions having a maximum diameter of 7 mm distributed over the volume as depicted in Fig. 1(b). The inclusions were filled with the same mixture as the background to obtain homogeneous measurements, and a liquid absorber was added to create a contrast of 8× for objects II and III, and 4× for object I for heterogeneous measurements. The phantom was illuminated over a 45 mm by 35 mm surface with a wide-field source created using a Ti-sapphire laser operating at 700 nm coupled to digital micromirror device (DMD) via a beam expander. The transmitted modulated time-resolved light was detected with an ultra-fast gated CCD camera. The acquisition parameters of the camera were set to 300 ps gates at 40 ps intervals with a high voltage of 510 V. The overall time of acquisition for 36 illumination patterns was less than 12 min.

Examples of typical detector readings for the homogeneous simulations are provided in Fig. 2. They correspond to the central excitation source/pattern and the central detector/pattern, respectively. The Jacobians in the normalized Born scheme associated with these detector readings for the three time gates considered *in silico* are provided in the same figure. In this study, we selected the maximum, half-rising, and half-decaying gates. The gates selection is performed independently for each pattern–detector pair on the homogeneous forward simulation. Thus, for instance, two gates associated with the maximum of the curve can occur at different absolute times for different pattern–detector pairs.

In all cases presented, the detector readings display the marked temporal features of temporal point spread functions (TPSF). The use of patterned excitation and/ or detection leads to a temporal broadening of the TPSFs (TPSF FWHM: • + • = 540.5 ps; □ + • = 576 ps; □ + ⊡ = 576.4 ps) but do not smear significantly the detected photon's time-of-flight statistics. The broadening of the temporal information, associated to the larger volume probed by the detected photons in this configuration, is clearly depicted in the Jacobian spatial distribution. As seen in Fig. 2, the Jacobians associated with early gates (half-rising maximum), are sensitive to large volumes when wide-field structured light is employed to the extent that few differences can be identified by direct visual comparison of the □ + ⊡ Jacobians for the three gates investigated.

Figure 3 shows a comparison of the optical reconstructions based on these time-resolved data sets. For a similar data set size, □ + • strategy outperforms • + • both in quantification and resolution, whereas • + • and □ + ⊡ offer relatively similar performances. Even though □ + ⊡ is characterized by spatially extended Jacobians, the optical reconstructions based on this strategy allows for quantitative three dimensional imaging as depicted in Fig. 3(c).

These simulations are further validated by the experimental investigation employing the same wide-field pattern strategy using the murine model phantom shown in Fig. 1(b). An example of 3D experimental reconstructions for absorption heterogeneities is shown in Fig. 4. In this investigation, we were limited to wide-field strategies as it was not possible to concurrently acquire point excitation and wide-field excitation data with our current instrument. Note also that the patterned detection scheme was obtained from the same data sets by applying integrating masks on the CCD camera output. However, wide-field pattern detection can be performed with one single detector associated with a second DMD in the detection optical chain [8]. The benefits are then on the instrumental side: cost, use of a more sensitive detector (such as a photomultiplier tube), potential for spectral multiplexing, etc.

Table 1 summarizes a quantitative assessment of the different experimental strategies investigated. We computed two metrics based on the 3D reconstruction. First, a quantitative accuracy metric calculated as the error in the mean absorption coefficient reconstructed over the 50% isovolume versus the known value was computed. Second, a resolution metric, defined as the estimated reconstructed radius of the cylindrical object reconstructed compared to the true radius of the objects (7 mm), was estimated.

In all the cases investigated, the three objects were resolved in the reconstructions. The □ + • with time-gated (TG) data sets provided more accurate reconstructions than their CW equivalents. Thus, even with extended illumination/detection strategies, the additional information provided by TG data types was retained and allowed for higher fidelity reconstructions than CW data types. In particular, the improvement in resolving the depth information is clearly demonstrated in the reconstruction of object III. As expected from *in silico* simulations, the experimental reconstructions based on illumination and detection patterns were characterized by a poorer resolution and quantification. Only in the case of object I, □ + • was less quantitatively accurate, as object I was over reconstructed, leading to a smaller reconstructed diameter and, hence, a higher mean absorption than expected. Finally, simple patterns were used in this work due to their experimental ease to implement. However, such patterns are not expected to provide the optimal information content. A significant increase in the reconstructions fidelity is expected when employing more efficient spatial patterns, such as Fourier modes.

In conclusion, we have demonstrated *in silico* and experimentally, for the first time to our knowledge, the feasibility of performing DOT based on time-domain data sets with wide-field patterned illumination and detection strategies. We have validated the potential of the technique based on TG data sets and for absorption heterogeneities, but the technique can be extended to any time-resolved data sets and contrast functions. We expect these new experimental strategies to profoundly affect time-resolved studies of thick tissue by providing dense spatial, temporal, and potentially spectral data sets for quantitative high-resolution volumetric imaging at unmatched speed.

Acknowledgments

X. Intes gratefully acknowledges the technical support of the Computational Center for Nanotechnology Innovations (CCNI) at RPI. F. Lesage is supported by a Natural Sciences and Engineering Research Council of Canada (NSERC) Discovery Grant.

References

1. Intes X, Djeziri S, Ichalalene Z, Mincu N, Wang Y, St-Jean P, Lesage F, Hall D, Boas D, Polyzos M, Fleiszer D, Mesurolle B. Acad Radiol. 2005; 12:934. [PubMed: 16023382]
2. Tromberg BJ, Pogue BW, Paulsen KD, Yodh AG, Boas DA, Cerussi AE. Med Phys. 2008; 35:2443. [PubMed: 18649477]
3. Strangman G, Boas DA, Sutton JP. Biol Psychiatry. 2002; 52:679. [PubMed: 12372658]
4. Intes X, Chance B. Radiol Clin N Am. 2005; 43:221. [PubMed: 15693658]
5. Cuccia DJ, Bevilacqua F, Durkin AJ, Ayers FR, Tromberg BJ. J Biomed Opt. 2009; 14:024012. [PubMed: 19405742]
6. Lukic V, Markel V, Shcotland JC. Opt Lett. 2009; 34:983. [PubMed: 19340192]
7. Bassi A, D’Andrea C, Valentini G, Cubeddu R, Arridge S. Opt Lett. 2009; 34:2156. [PubMed: 19823533]
8. Belanger S, Abran M, Intes X, Casanova C, Lesage F. J Biomed Opt. 2010; 15:016006. [PubMed: 20210452]
9. Chen J, Intes X. Opt Express. 2009; 17:19566. [PubMed: 19997176]

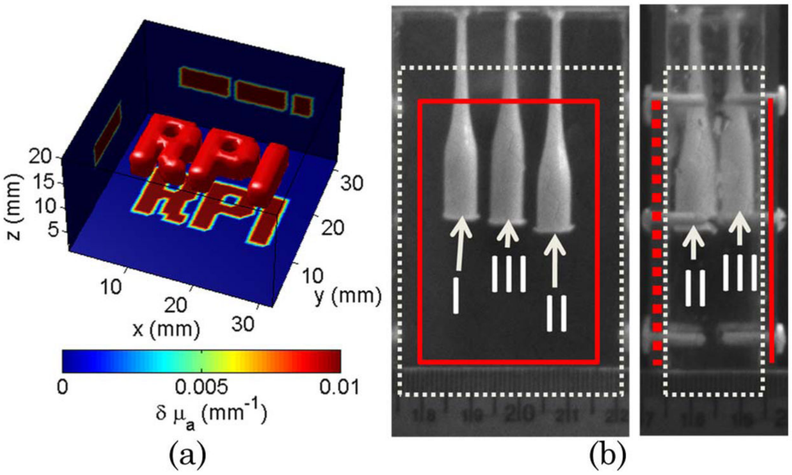

Fig. 1.

(Color online) (a) *In silico* phantom with complex absorptive structure. (b) Experimental phantom with three absorptive inclusions. The solid line (red) corresponds to the illuminated surface and point detector distribution. The dotted lines (white) delineate the reconstructed volume.

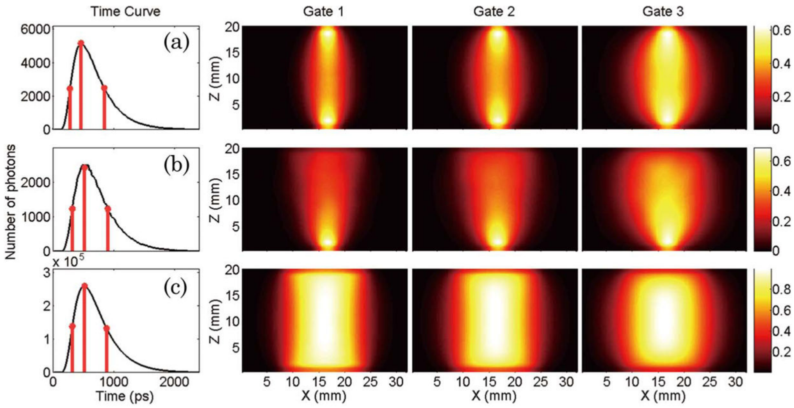

Fig. 2.

(Color online) Simulated detector readings for the central source–pattern and associated Jacobians for the three gates selected: (a) point source–point detector (• + •), (b) patterned illumination–point detector (□ + •), and c) patterned illumination–patterned detection (□ + ⊡).

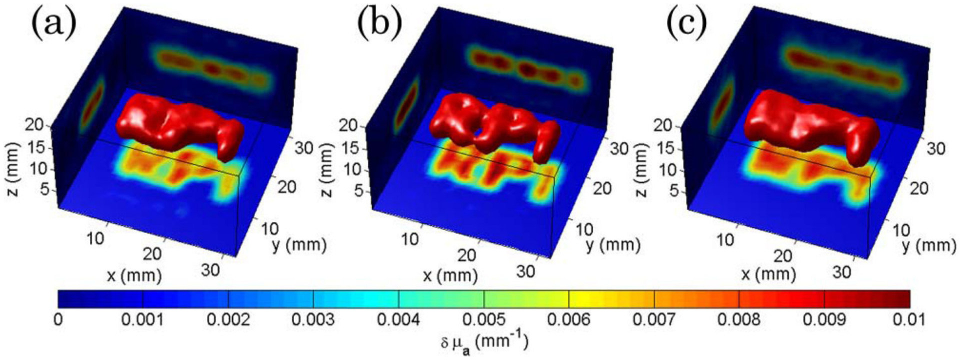

Fig. 3.

(Color online) Optical reconstructions of the phantom of Fig. 1(a) for (a) point source–point detector time-gated data, (b) patterned excitation–point detector, and (c) patterned excitation–patterned detector. The isovolume was set at 40% of the maximum reconstructed value. The projections of the central reconstructed plane are provided on each boundary for each case.

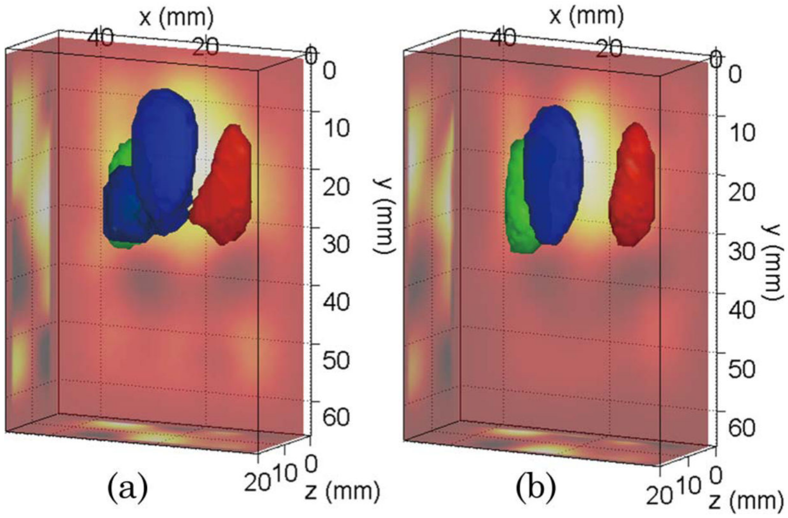

Fig. 4.

(Color online) Optical reconstructions of the phantom of Fig. 1(b) for the pattern source–point detector strategy: (a) CW data and (b) TG data. The isovolume was set at 50% of the maximum reconstructed value. The ray–sum projections are provided on the sides of the reconstructed volume.

Table 1

Quantitative and Resolution Errors in the 3D Reconstructions Compared to the Known Values of the Experimental Heterogeneities

		Estimation Error (%)			**Diameter (mm)**		
		Incl 1	**Incl 2**	**Incl 3**	**Incl 1**	**Incl 2**	**Incl 3**
Pattern	TG	−30.3	3.6	2.7	6.6	7.8	9.1
+ Point	CW	17.7	5.3	26.1	8.0	8.4	14.1
Pattern	TG	6.5	42.4	17.5	17.1	14.8	14.1
+ Pattern	CW	31.9	57.7	32.9	14.6	16.6	11.4